FULL PAPER

Electrical Manipulation of Orbital Occupancy and Magnetic Anisotropy in Manganites

Bin Cui, Cheng Song,* Gillian A. Gehring, Fan Li, Guangyue Wang, Chao Chen, Jingjing Peng, Haijun Mao, Fei Zeng, and Feng Pan*

Electrical manipulation of lattice, charge, and spin is realized respectively by the piezoelectric effect, field-effect transistor, and electric field control of ferromagnetism, bringing about dramatic promotions both in fundamental research and industrial production. However, it is generally accepted that the orbital of materials are impossible to be altered once they have been made. Here, electric field is used to dynamically tune the electronic-phase transition in (La,Sr)MnO$_3$ films with different Mn^{4+}/(Mn^{3+} + Mn^{4+}) ratios. The orbital occupancy and corresponding magnetic anisotropy of these thin films are manipulated by gate voltage in a reversible and quantitative manner. Positive gate voltage increases the proportion of occupancy of the orbital and magnetic anisotropy that were initially favored by strain (irrespective of tensile and compressive), while negative gate voltage reduces the concomitant preferential orbital occupancy and magnetic anisotropy. Besides its fundamental significance in orbital physics, these findings might advance the process towards practical oxide-electronics based on orbital.

1. Introduction

A wide variety of experimental and theoretical investigations have been pursued intensively to control the performance of materials at the atomic, or even subatomic level for a long period of time.[1–3] The interaction between lattice, charge, spin, and orbital degrees of freedom is found to play a direct and crucial role in the performance of electronic materials, displaying a rich spectrum of exotic phenomena.[4–6] The electric field effect with advantages of low power consumption and high controllability offers an effective and reversible route to confine the lattice, charge, and spin (as illustrated in **Figure 1**): a) the piezoelectric effect in crystalline materials without inversion symmetry has bridged electric field and lattice for more than 130 years;[7] b) the field-effect transistor (FET) provided

a classic model for the manipulation of carrier density by electrical means, constituting the cornerstone of the semiconductor industry;[8] c) the magnetization switching is driven reversibly by applied electric fields, which is expected to have a great technological impact on information storage.[9,10] However, electrical control of the missing member—orbital degree of freedom, whose small perturbations would lead to giant responses in the electric and magnetic properties[11,12]—has thus far remained an interesting concept lacking experimental insight.

The orbital represents the shape of electron cloud.[13] In mixed-valence manganites, the occupancy of the d orbital controls the magnitude and anisotropy of the interatomic electron-transfer interaction and hence exerts a key influence on the chemical bonding and physical properties.[4,13] For example, orbital occupancy tunes the magnetic behaviors of manganites with the help of strain design, persistently associated with several antiferromagnetic (AF) structures.[14,15] However, the lattice distortion inevitably introduces impurities and extra scattering centers to the system, which are irreversible and hardly controllable, and the orbital occupancy is fixed once the materials have been made and put into use. Application of the FET principle to achieve doping variation has modulated the magnetic or electric performances and phase transition in manganites,[16,17] which is expected to provide an approach to tune orbital occupancy reversibly. The main technological challenge for measuring the change of the orbital occupancy under the influence of an electric field is that the detection of orbital occupancy using X-ray linear dichroism (XLD), calls for an exposed sample with a robust remanent electric field effect,[18] which cannot be achieved by conventionally electrostatic modification of carrier density.[10,11] Fortunately, the relaxation of the gating effect generated by ionic liquid in manganites is negligible even after gate voltage is turned off, guaranteeing ex situ measurements of the orbital.[19]

2. Results and Discussion

A series of 20 nm thick (La,Sr)MnO$_{3-\delta}$ films with different $x = $ Mn^{4+}/(Mn^{3+} + Mn^{4+}) were prepared by pulsed laser deposition (PLD) at various oxygen background (cooling) pressures of 200 mTorr (300 Torr) ($x = 0.54$), 100 mTorr (100 Torr)
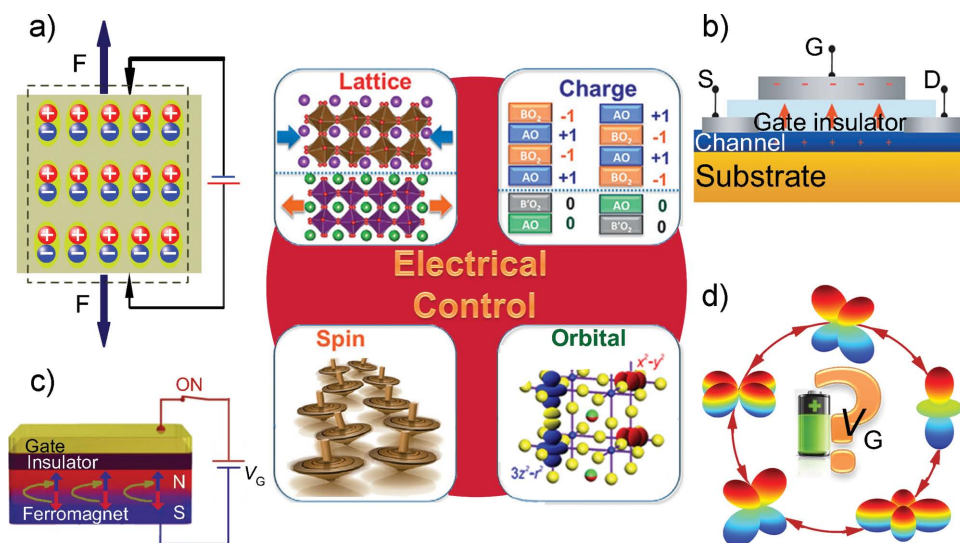
B. Cui, Dr. C. Song, F. Li, G. Y. Wang, Dr. C. Chen,
J. J. Peng, H. J. Mao, Dr. F. Zeng, Prof. F. Pan
Key Laboratory of Advanced Materials (MOE)
School of Materials Science & Engineering
Tsinghua University
Beijing 100084, China
E-mail: songcheng@mail.tsinghua.edu.cn;
panf@mail.tsinghua.edu.cn
Prof. G. A. Gehring
Department of Physics and Astronomy
University of Sheffield
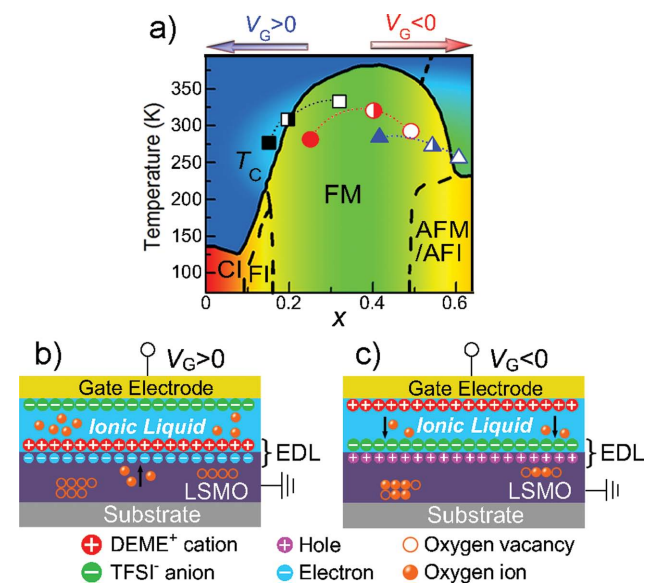Hicks Building, Sheffield S3 7RH, UK

Figure 1. a) Electric field-induced polarization and corresponding lattice deformation in piezoelectric materials; b) The manipulation of carrier density in FET by electric field; c) Electric field controls the magnetization switching in magnetic materials; d) The conception of electrical manipulation of orbital.

($x = 0.41$), and 50 mTorr (10 Torr) ($x = 0.20$) on STO substrate (Supporting Information Figure S1). The electronic phase diagram of $(La,Sr)MnO_{3-\delta}$ is drawn as a function of $x = Mn^{4+}/(Mn^{3+} + Mn^{4+})$, as shown in **Figure 2**a, where x could be controlled by the Sr concentration,[4] oxygen pressure during film growth,[18] and gate voltage (V_G).[20] We investigate samples of $(La,Sr)MnO_{3-\delta}$ (LSMO) grown with initial x values of 0.54,

Figure 2. a) Electronic phase diagram of $(La,Sr)MnO_3$ with varying $x = Mn^{4+}/(Mn^{3+} + Mn^{4+})$ ratio. The half-filled triangle, circle, and square denote the positions of samples on STO with initial $x = 0.54$, 0.41, and 0.20 in phase diagram, respectively. The sample positions after applying positive and negative V_G are marked by corresponding filled and empty symbols. The abbreviations stand for spin-canted insulating (CI), ferromagnetic insulating (FI), ferromagnetic metal (FM), antiferromagnetic metal (AFM), and antiferromagnetic insulating (AFI) phase, respectively. Schematic illustration of the effect of electric double layer (EDL) with b) $V_G > 0$ and c) $V_G < 0$.

0.41, and 0.20. These are shown as a half-filled triangle, circle, and square respectively in Figure 2a. This experimental design locates them close to the boundary between ferromagnetic metallic (FM) and antiferromagnetic metallic or insulating (AFM or AFI) phase, in the center of the FM phase and at the boundary between FM and insulting [spin-canted insulating (CI) and ferromagnetic insulating (FI)] phase, respectively.

We manipulate the electrical phase transition and Mn e_g orbital occupancy in $(La,Sr)MnO_{3-\delta}$ with different initial x by applying gate voltage through ionic liquid. Unlike the electrostatic manipulation of carrier density in $(Ga,Mn)As$,[21] the electric fields created by the electric double layer (EDL) on a manganite under positive V_G are sufficiently high to change the chemical composition, in this case by driving oxygen ions out of the oxides (Figure 2b).[19,20] This is accompanied by the injection of electrons into films and moves the sample to a lower x as the left arrow shows in Figure 2a. On the contrary, negative V_G extracts electrons with O^{2-} ions migrating back to the films (Figure 2c), increasing the x in LSMO (the right arrow in Figure 2a). When gate voltage is large enough (e.g., +3 V or −3 V), the gating effect based on oxygen migration is stable at room, or lower temperatures with negligible relaxation even after V_G is turned off (Supporting Information Figure S2) that enables us to determine the x values, magnetic and electric properties of samples ex situ regardless of the atmosphere. Although the oxygen vacancies migration is not directly observed, the Mn valence variation in X-ray photoelectron spectroscopy (XPS) and microstructure evolution in HRTEM under different gate voltages suggest the formation and annihilation of oxygen vacancies.[22] This is also supported by the demonstration of oxygen vacancies-based conduction filaments for resistive switching behaviors, based on the cutting-edge nanocharacterization methods[23,24] and theoretical calculations.[25]

We plot the variations of the concentration x determined by XPS (Supporting Information Figure S1), where the full and empty symbols represent the values of x that they reach at voltage of +3 and −3 V, respectively. The heights of the symbols

Table 1. Curie temperature (T_C) and the composition (x) of tensile strained $(La,Sr)MnO_{3-\delta}$ under various V_G.

V_G [V]	−3	0	+3
initial $x = 0.54$ (triangles) (T_C/x)	260 K/0.64	271 K/0.54	275 K/0.43
initial $x = 0.41$ (circles) (T_C/x)	288 K/0.47	315 K/0.41	275 K/0.25
initial $x = 0.20$ (squares) (T_C/x)	331 K/0.30	305 K/0.20	279 K/0.15

on this plot represent the measured temperature values of the metal–insulator transition as obtained from resistance–temperature (R–T) curves (Supporting Information Figure S3). The values of the transition temperatures (equal to Curie temperature, T_C) and corresponding x are given in **Table 1** and follow what is expected from the phase diagram. For the case of initial $x = 0.54$, negative V_G drives the sample into the AFM or AFI phase, accompanied by decreased T_C, while positive V_G favors the FM phase with the enhancement of T_C. When initial $x = 0.41$, the sample is at the FM-phase region with optimally magnetic and conductive performances. Hence, both positive and negative voltages result in an abrupt decay of conductivity and T_C. In contrast, the magnetic properties of samples with initial $x = 0.20$, are enhanced or suppressed by negative or positive V_G, respectively. In conjunction with the growth oxygen pressure and gate voltage, we approximately replicate the dependence of T_C on x in classic phase diagram using a given stoichiometric target. Note that, this phase transition is bulk effect instead of surface carrier accumulation according to the directly microcosmic observation and Mn $2p$ XPS depth profiling in our previous work.[22] Compared with the electrostatic manipulation based on the capacitance of EDL,[26] the change of x in our system is rather large as the variation of oxygen vacancies is sensitive to the external electric field.

We now address the question how the orbital occupancy varies under the electric field. In this part, we concentrate primarily on the sample with $x = 0.54$ because such a nearly half-doped manganite is extremely sensitive to external stimuli, like an electric field.[27] A tensile strain is produced by growing samples on $SrTiO_3$ (STO, $\varepsilon = 0.9\%$) and a compressive strain by growing on $LaAlO_3$ (LAO, $\varepsilon = -2.1\%$). The orbital occupancy is measured by XLD which is the difference between the normalized XAS with photon polarization parallel (E//a) and almost perpendicular (E//c) to the sample plane. The measurement temperature for XLD is 300 K as the interference from ferromagnetism is negligible at a comparatively high temperature, enhancing the accuracy of the XLD signals.[18] The spectra normalization was made by dividing the spectra by a factor such that the L_3 pre-edge and L_2 postedge have identical intensities

for the two polarizations. After that, the pre-edge spectral region was set to zero and the peak at the L_3 edge was set to one. XLD is the difference between the two measurements. Irrespective of the surface symmetry breaking in such a thick films of 20 nm, the area under XLD around the L_2 peak (647.5–660.0 eV, the shadowy areas in **Figure 3**) could be used to roughly represent the difference between the relative occupancies of $3z^2 - r^2$ [$P(3z^2 - r^2)$] and $x^2 - y^2$ [$P(x^2 - y^2)$] orbital: $A_{XLD} = P(3z^2 - r^2) - P(x^2 - y^2)$ (more details in Supporting Information).[18,28] For tensile strained LSMO without gate voltage, $x^2 - y^2$ orbital is favored with a negative A_{XLD}, while the $3z^2 - r^2$ orbital is stabilized ($A_{XLD} > 0$) once compressive strain is applied.

The XAS and the concomitant XLD for the tensile (STO) and compressive (LAO) strained LSMO under representative V_G are presented in Figure 3a,b, respectively. The most eminent feature observed here is that the usage of $V_G = -3$ V, pulls down the absolute value of A_{XLD} while $V_G = +3$ V does the opposite, as presented in Figure 3 and summarized in **Table 2**. The $x^2 - y^2$ orbital occupancy is strongly weakened by negative V_G but dramatically enhanced by positive one in tensile strained LSMO: $P(x^2 - y^2) = 53.1\%$, 57.8%, and 60.2% for $V_G = -3$, 0, and +3 V, respectively. A similar tendency is also found in tensile strained samples of $x = 0.41$ and 0.20 (Supporting Information Figure S4). When the strain turns to be compressive, V_G of −3 V breaks somehow the $3z^2 - r^2$ orbital occupancy with $P(3z^2 - r^2) = 51.3\%$ compared to $P(3z^2 - r^2) = 55.1\%$ for $V_G = 0$ V, while $V_G = +3$ V stabilizes the $3z^2 - r^2$ orbital with enhanced
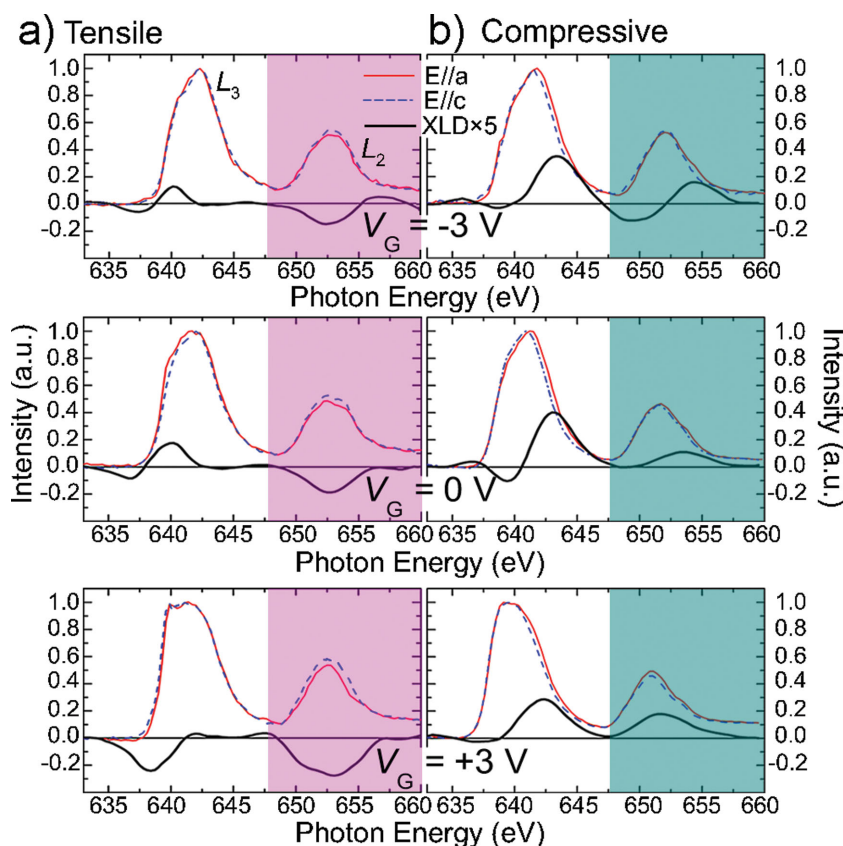
Figure 3. Normalized XAS [photon polarization parallel (E//a) and almost perpendicular (E//c) to the sample plane] and XLD signals of a) tensile and b) compressive strained LSMO.

Table 2. The composition (x), A_{XLD}, magnetic properties, and orbital mixing angle θ of tensile and compressive strained LSMO (initial $x = 0.54$) at various V_G.

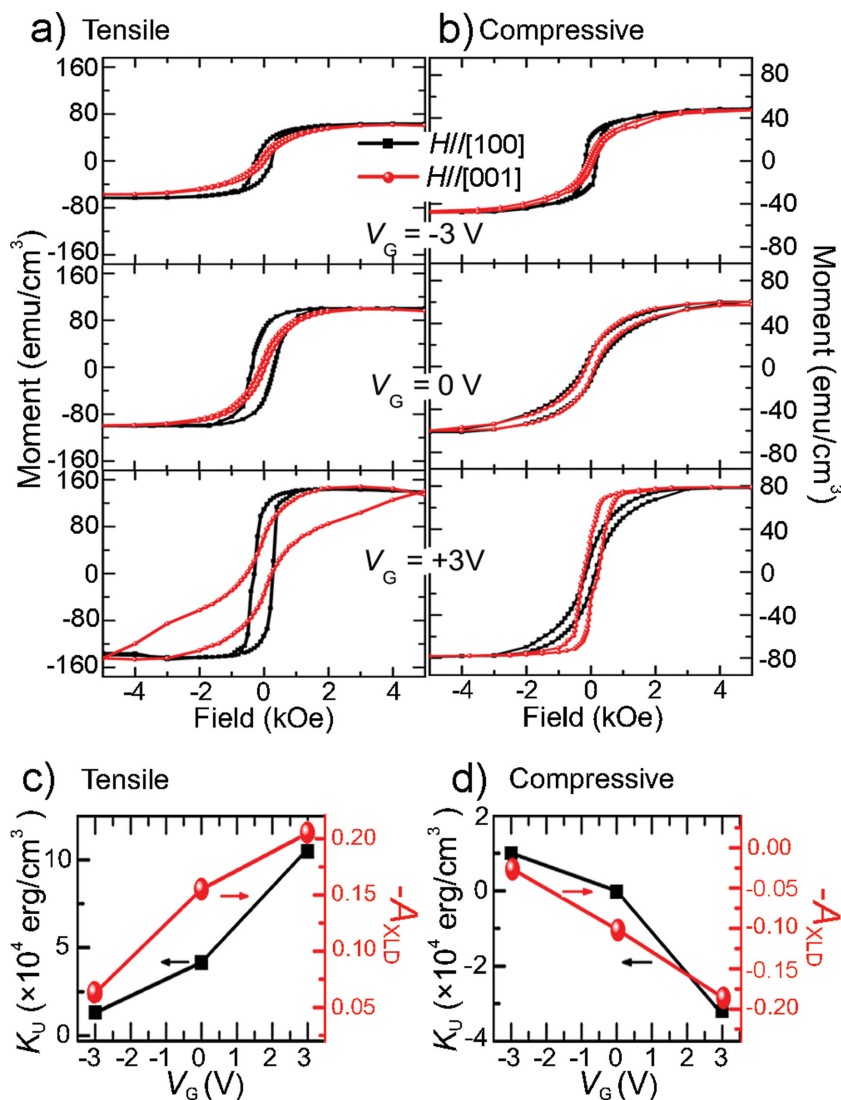| V_G [V]	Tensile			Compressive		
	−3	0	+3	−3	0	+3
x	0.64	0.54	0.43	0.63	0.53	0.43
A_{XLD}	−0.063	−0.155	−0.205	0.026	0.102	0.186
M_S (emu/cm³)	61.6	99.2	143.2	47.2	59.2	78.4
K_U (×10⁴ erg cm⁻³)	1.3	4.1	10.6	1.0	0.0	−3.3
θ [°]	93.66	98.97	101.88	88.52	84.17	79.29

$P(3z^2 - r^2)$ of 59.3%. It is then concluded that positive or negative voltage strengthens or weakens preferential orbital occupancy, respectively. Although it is difficult to change the orbital occupancy fundamentally and the variations of A_{XLD} are relatively small, the clearly detected signals illustrate the high sensitivity of the orbital occupancy to gate voltage. The magnitude of the variation of orbital occupancy in our case is much larger than that of the calculated value relevant to interfacial ferroelectric polarization.[12] Also, the modulation of x value is uniform from the surface to bottom of film according to the XPS depth profile, which is also supported by the random nucleation model in ionic liquid-gated LSMO.[22] Thus, the changes in orbital occupancy are almost constant in the whole film rather than limited at the interface or surface.

The origin of electrical manipulation is the cooperative effect of strain and superexchange. When positive gate voltage is applied, oxygen vacancies in LSMO are increased with injection of electrons and all the samples still locate in the metallic phase, where the e_g doublet is split into a lower and an upper energy orbital due to the strain. The injected electrons fill the orbital starting from the one with lowest energy, that is $x^2 - y^2$ for tensile strain (STO) and $3z^2 - r^2$ for compressive strain (LAO), inducing the enhancement of preferential orbital occupancy. In contrast, negative gate voltage increases the x value with oxygen ions migration into LSMO, which favors the superexchange in doped manganites.[4] The strong superexchange would result in the suppression of electron-transfer interaction and preferential orbital occupancy,[13] corresponding to the small A_{XLD} in Figure 3. Thus, the preferential e_g orbital occupancy is enhanced by positive V_G while broken by negative one, which can be readily generalized to other correlated oxide heterostructures with preferential orbital occupancy, such as VO₂/TiO₂.[29] We also note that unlike the intrinsic preferential orbital occupancy phase in the classic phase diagram describing the bulk LSMO, the in-plane orbital occupancy of tensile-strained samples at $V_G = +3$ and −3 V are enhanced and reduced, respectively, compared to that of the bulk LSMO with the identical x, producing a state with a slightly different orbital occupancy from the classic-phase diagram.

For La₁₋ᵧSrᵧMnO₃₋δ, the Mn can be written as Mn_x^{4+} and Mn_{1-x}^{3+}. It is easy to show that $x = y − 2\delta$. In this scenario, introducing oxygen vacancies automatically changes the value of x and hence the phase of LSMO.[30] As a result, the influences of oxygen vacancies δ and Sr-doping concentration y on the performance of LSMO almost overlap, collectively reflecting in the variation of x. A closer inspection shows that there are

differences in T_C between our samples and the classic phase diagram in Figure 2a: the sample (initial $x = 0.54$) on STO shows the T_C at $V_G > 0$ and $V_G < 0$ lower and higher than their bulk counterparts, respectively. This difference could arise from two possible origins: additional effect of oxygen vacancies and varied preferential orbital occupancy. Note that positive V_G introduces oxygen vacancies both in the samples with $x = 0.20$ and 0.54, but results in respectively higher and lower T_C compared with the phase diagram, suggesting that the additional effect of oxygen vacancies should not dominate the performance discrepancy between our samples and the phase diagram, though it cannot be firmly ruled out. Instead, the varied preferential orbital occupancy is most likely the main source responsible for the difference. Additionally, our previous work shows that the T_C of the pristine (La,Sr)MnO₃ with in-plane preferential orbital occupancy on STO is around 50 K higher than that on LAO whose preferential orbital occupancy is out of plane, suggesting the importance of orbital occupancy on controlling the magnetic performance.[18]

The magnetic switching behavior and magnetic anisotropy under different V_G should be sensitive to the variation in e_g orbital occupancy and carrier density.[15,21,31] We estimate the anisotropy of LSMO by the effective anisotropy constant $K_U = H_A M_S / 2$, where H_A is the difference of the saturated fields between [100] and [001] axes (**Figure 4**a,b), and M_S is the saturated magnetization. The magnetic properties are measured at 10 K, as the form of the magnetic anisotropy is not temperature dependent but its magnitude is increased at low temperatures.[32] Since we do not quantitatively correlate the magnetization and orbital occupancy, the measurements carried out at different temperatures are acceptable. As expected, both shape anisotropy and in-plane orbital occupancy leads the pristine tensile strained sample ($V_G = 0$ V) to exhibit an in-plane magnetic anisotropy with a K_U of 4.1 × 10⁴ erg cm⁻³ (Table 2). By applying gate voltage, only the orbital-dependent magnetic anisotropy is manipulated. Positive voltage of +3 V seriously reduces the magnetization switching out-of-plane, resulting in $K_U = 10.6 × 10^4$ erg cm⁻³, in contrast to V_G of −3 V corresponding to $K_U = 1.3 × 10^4$ erg cm⁻³. The K_U of $V_G = +3$ V ($x = 0.43$) is much larger than that of the pristine sample with initial $x = 0.41$ ($K_U = 5.8 × 10^4$ erg cm⁻³), though their compositions are quite close, suggesting that the electrical manipulated e_g orbital occupancy produces a dramatic change in the magnetic anisotropy (Supporting Information Figure S5). When the LSMO changes to be compressive strained (Figure 4b), no detectable magnetic anisotropy is observed in the pristine sample, which can be explained by the competitive result of e_g orbital occupancy and shape anisotropy. This balance is easy to be broken by a perturbation: V_G of −3 V introduces an easy axis in [100] with a K_U of 1.0 × 10⁴ erg cm⁻³, while $V_G = +3$ V makes the film behave as perpendicular magnetic anisotropy with a negative K_U of −3.3 × 10⁴ erg cm⁻³. Remarkably, combinations of V_G dependent −A_{XLD} and K_U in Figure 4c,d confirm that the increased (decreased) in-plane orbital occupancy at positive (negative) V_G strengthens (weakens) the magnetic anisotropy of LSMO with the [100] easy axis, while the enhanced $3z^2 − r^2$ orbital occupancy in compressive strained LSMO as V_G changes from −3 to +3 V would change the easy axis of LSMO from in-plane to out-of-plane, gradually.

ADVANCED
FUNCTIONAL
MATERIALS
www.afm-journal.de

Materials
Views
www.MaterialsViews.com

Figure 4. Magnetization curves measured with field along [100] and [001] directions of LSMO with a) tensile and b) compressive strain under different V_G. The dependence of K_U (left axis) and $-A_{XLD}$ (right axis) on V_G for the case of c) tensile and d) compressive strain.

In addition to magnetic anisotropy measurements, we have explored gate voltage-dependent saturation magnetization, which is not so robust because the films under various V_G are close the boundary between FM and AFM/AFI phases. Positive V_G of +3 V drives the pristine sample on STO with $x > 0.4$ from the AFM or AFI scale to the FM-phase region in phase diagram (Figure 2a), as the injection of electrons favors the double exchange effect, apparently enhancing the M_S though the preferential e_g orbital occupancy is increased in this case. Corresponding values for $x = 0.54$ are listed in Table 2. In stark contrast, for the case of −3 V, extraction of electrons pulls the sample deeper into the antiferromagnetic phase with ferromagnetism suppression. For compressive strained LSMO, the magnetization exhibits a similar dependence on V_G that $M_S = 47.2, 59.2$, and 78.4 emu cm^{-3} for $V_G = -3, 0$, and +3 V, respectively. It is generally accepted that the e_g orbital occupancy induced by the strain effect in manganite films inevitably deteriorates the ferromagnetic ordering

and conductivity, which has been an obstacle for the integration of manganites into spintronics.[15] The increased preferential e_g orbital occupancy associated with magnetization and conductivity enhancements for electrical manipulation of ferromagnetism in the present case reaffirms the difference between electrically manipulated and bulk LSMO with the same x, providing a promising way for the introduction of strong magnetic anisotropy without the cost of relevant magnetic and electric properties. It is useful to point out that the enhancement of magnetic anisotropy would reduce the width of domain wall, likely enhancing the domain wall resistance (more details in Supporting Information).[33–35]

The relationship between the variations of orbital occupancy, magnetic anisotropy, and magnetization could be understood from the perspective of orbital mixing. The measurements of the XLD and the values of orbital occupancy were made at room temperature when the samples were above, or very close to, their ordering temperature, where the carriers in the samples will be polarons. Thus, the e_g band states would be combinations of the states given by Equations 1 and 2:[36]

$$|\psi_{low}\rangle = \cos\frac{\theta}{2}|3z^2 - r^2\rangle + \sin\frac{\theta}{2}|x^2 - y^2\rangle \quad (1)$$

$$|\psi_{high}\rangle = \sin\frac{\theta}{2}|3z^2 - r^2\rangle - \cos\frac{\theta}{2}|x^2 - y^2\rangle \quad (2)$$

where $|\psi_{low}\rangle$, $|\psi_{high}\rangle$, $|3z^2 - r^2\rangle$, and $|x^2 - y^2\rangle$ are the wave functions of low, high energy states, $3z^2 - r^2$, and $x^2 - y^2$ orbital, respectively. The mixed orbital is the hybridization of $3z^2 - r^2$ and $x^2 - y^2$ orbital, whose proportions $P(3z^2 - r^2)$ and $P(x^2 - y^2)$, respectively, are obtained from XLD results. Then the angle of orbital mixing for low energy state can be calculated from $P(3z^2 - r^2) = \cos^2\frac{\theta}{2}$ and $P(x^2 - y^2) = \sin^2\frac{\theta}{2}$, according to the normalization and orthogonality of orbital hybridization. In manganites, the magnetization is determined by the bandwidth while the electron transfer integrals depend on the mixing angle θ.[37] For an unstrained magnetite in the metallic regime $\theta = 90°$, so that $P(x^2 - y^2) = P(3z^2 - r^2)$; this corresponds to maximum transfer integrals between the Mn ions. In the films grown on STO that are under tensile strain the nearest neighbors separation will be greater in the plane.

The values of θ measured in our experiments, shown in Table 2, are all relatively close to 90°. The θ values of films grown on STO are all larger than 90°, corresponding to a higher probability $P(x^2 - y^2)$, while those grown on LAO have a higher probability $P(3z^2 - r^2)$ with $\theta < 90°$. Thus, for the orbital where the nearest neighbor separations are reduced by

Materials
Views
www.MaterialsViews.com

ADVANCED
FUNCTIONAL
MATERIALS
www.afm-journal.de

FULL PAPER

the strain, their occupations are enhanced, in-plane for tensile strain (STO) and out-of-plane for compressive strain (LAO). Positive V_G introduces electrons into the orbital enhanced by strain, giving rise to a larger value of $|\theta - 90°|$. While negative V_G increase the x value with stronger superexchange effect, which drives the value of θ close to 90°. It is also clear from this table that the magnitude of $|\theta - 90°|$ increases as the saturation magnetization increases. In the ferromagnetic phase, much of the stabilization energy of the magnetization comes from the increase in the bandwidth in the partially occupied e_g band due to efficient electron transfer between Mn ions facilitated by the parallel spin electrons in the Mn t_{2g} shell.[4] This increase in $|\theta - 90°|$ corresponds to an enhancement of the transfer integrals along the directions where the distortions are reducing the Mn–Mn spacing. Hence, we can understand the orbital enhancement in these films in terms of the benefits of increasing the transfer integrals when the spin ordering allows this effect to increase the bandwidth. The induced preferential orbital occupancy naturally impacts on the magnetic anisotropy. The enhancement of $P(x^2 - y^2)$ as the voltage reduces the value of x from 0.64 to 0.43 leads to a strong uniaxial anisotropy for the film grown on STO under a voltage of +3 V. A different effect is seen for the film grown on LAO: the anisotropy is in-plane for a voltage of −3 V but this is reduced to zero at 0 V and then becomes out-of-plane as +3 V is applied with increased magnetization.

3. Conclusions

In conclusion, an electrical manipulation of phase transition and orbital occupancy in LSMO is realized by applying gate voltage in a reversible and quantitative manner, generating a discrepant state with different orbital occupancy but the same $Mn^{4+}/(Mn^{3+} + Mn^{4+})$ compared to the bulk. For negative V_G, the extraction of electrons drives LSMO into the AFM/AFI phase accompanied with uniform orbital occupancy, orbital mixing angle close to 90°, and reduced magnetic anisotropy. On the contrary, when V_G is positive, electrons are injected into strain-stabilized orbital of LSMO, driving the mixing angle away from 90°. For the manganite films near the antiferromagnetic phase, positive gate voltage could simultaneously enhance the magnetic anisotropy and magnetization. In the case of preferential orbital occupancy and the concomitant magnetic anisotropy, we have seen that the control of x using voltage has additional benefits (simultaneous higher magnetization and anisotropy) more than could be obtained by growth parameters alone. Although the difficulty of handling ionic liquid, our findings present a broad opportunity to advance the control of orbital in a variety of correlated electron system.

4. Experimental Section

Sample Preparation: 20 nm thick $(La,Sr)MnO_{3-\delta}$ films were grown using PLD from a stoichiometric $La_{0.6}Sr_{0.4}MnO_3$ target by applying a KrF excimer laser at a rate of 0.77 nm min^{-1}. STO ($a_{STO} = 3.90$ Å) and LAO ($a_{LAO} = 3.79$ Å) substrates are used to introduce tensile and compressive strain, respectively. The growth was monitored in situ by reflection high-energy electron diffraction analysis allowing precise control of the thickness at the unit cell scale and accurate characterization of the growth dynamics. The $Mn^{4+}/(Mn^{3+} + Mn^{4+})$ ratios of films are controlled by the oxygen pressure during growth and cooling process: when the growth (cooling) oxygen pressures are 200 (300 Torr), 100 (100 Torr), and 50 mTorr (10 Torr), the $Mn^{4+}/(Mn^{3+} + Mn^{4+})$ ratios are 0.54, 0.41, and 0.20, respectively.

Sample Characterization: Ionic liquid N,N-diethyl-N-(2-methoxyethyl)-N-methylammonium bis-(trifluoromethylsulfonyl)-mide with the freezing temperature of around 210 K was used as the electrolyte, whose irreversible reaction with manganites has been carefully ruled out[38] (Supporting Information Figures S6–7). Samples with large areas of 2.5 mm × 2.5 mm were entirely covered by ionic liquid with Au top electrodes and a specific voltage is applied between the Au electrode and $(La,Sr)MnO_3$ film by Agilent 2901A for about 30 min without special instruction. The values of x are determined by XPS at 300 K. XLD characterizations were performed in total electron yield mode at Beamline BL08U1A at Shanghai Synchrotron Radiation Facility. A superconducting quantum interference device was used to measure magnetic properties at 10 K. Before XPS, XLD, and magnetization measurements, the ionic liquid is removed by rinsing in acetone and alcohol. Conductivity was probed in a transistor structure (Supporting Information Figure S3) by the physical property measurement system.

Supporting Information

Supporting Information is available from the Wiley Online Library or from the author.

[1] H. Y. Hwang, Y. Iwasa, M. Kawasaki, B. Keimer, N. Nagaosa, Y. Tokura, *Nat. Mater.* **2012**, *11*, 103.

[2] M. Bibes, J. E. Villegas, A. Barthélémy, *Adv. Phys.* **2011**, *60*, 5.

[3] C. H. Ahn, A. Bhattacharya, M. D. Ventra, J. N. Eckstein, C. D. Frisbie, M. E. Gershenson, A. M. Goldman, I. H. Inoue, J. Mannhart, A. J. Millis, A. F. Morpurgo, D. Natelson, J. M. Triscone, *Rev. Mod. Phys.* **2006**, *78*, 1185.

[4] J. M. D. Coey, M. Viret, S. von Molnár, *Adv. Phys.* **1999**, *48*, 1673.

[5] E. Dagotto, *Rev. Mod. Phys.* **1994**, *66*, 763.

[6] B. Cui, C. Song, G. Y. Wang, H. J. Mao, F. Zeng, F. Pan, *Sci. Rep.* **2013**, *3*, 2542.

[7] J. Curie, P. Curie, *Bull. Soc. Minéral. France* **1880**, *3*, 90.

[8] J. E. Lilienfield, *Device for controlling electric current.* U.S. Patent 1900018, **1933**.

[9] H. Ohno, D. Chiba, F. Matsukura, T. Omiya, E. Abe, T. Dietl, Y. Ohno, K. Ohtani, *Nature* **2000**, *408*, 944.

[10] S. M. Wu, S. A. Cybart, P. Yu, M. D. Rossell, J. X. Zhang, R. Ramesh, R. C. Dynes, *Nat. Mater.* **2010**, *9*, 756.

[11] T. Maruyama, Y. Shiota, T. Nozaki, K. Ohta, N. Toda, M. Mizuguchi, A. A. Tulapurkar, T. Shinjo, M. Shiraishi, S. Mizukami, *Nat. Nanotechnol.* **2009**, *4*, 158.

[12] H. H. Chen, Q. Qiao, M. S. J. Marshall, A. B. Georgescu, A. Gulec, P. J. Phillips, R. F. Klie, F. J. Walker, C. H. Ahn, S. I. Beigi, *Nano Lett.* **2014**, *14*, 4965.

[13] T. Tokura, N. Nagaosa, *Science* **2000**, *288*, 462.

[14] E. Dagotto, *Science* **2005**, *309*, 257.

[15] C. Aruta, G. Ghiringhelli, V. Bisogni, L. Braicovich, N. B. Brookes, A. Tebano, G. Balestrino, *Phys. Rev. B* **2009**, *80*, 014431.

[16] A. S. Dhoot, C. Israel, X. Moya, N. D. Mathur, R. H. Friend, *Phys. Rev. Lett.* **2009**, *102*, 136402.

[17] T. Hatano, Y. Ogimoto, N. Ogawa, M. Nakano, S. Ono, Y. Tomioka, K. Miyano, Y. Iwasa, Y. Tokura, *Sci. Rep.* **2013**, *3*, 2904.

[18] B. Cui, C. Song, F. Li, G. Y. Wang, H. J. Mao, J. J. Peng, F. Zeng, F. Pan, *Sci. Rep.* **2014**, *4*, 4206.

[19] J. Jeong, N. Aetukuri, T. Graf, T. D. Schladt, M. G. Samant, S. S. P. Parkin, *Science* **2013**, *339*, 1402.

[20] I. H. Inoue, M. J. Rozenberg, *Adv. Funct. Mater.* **2008**, *18*, 2289.

[21] D. Chiba, M. Sawicki, Y. Nishitani, Y. Nakatani, F. Matsukura, H. Ohno, *Nature* **2008**, *445*, 515.

[22] B. Cui, C. Song, G. Y. Wang, Y. N. Yan, J. J. Peng, J. H. Miao, H. J. Mao, F. Li, C. Chen, F. Zeng, F. Pan, *Adv. Funct. Mater.* **2014**, *24*, 7233.

[23] J.-Y. Chen, C.-L. Hsin, C.-W. Huang, C.-H. Chiu, Y.-T. Huang, S.-J. Lin, W.-W. Wu, L.-J. Chen, *Nano Lett.* **2013**, *13*, 3671.

[24] F. Pan, S. Gao, C. Chen, C. Song, F. Zeng, *Mater. Sci. Eng. R* **2014**, *83*, 1.

[25] M. J. Rozenberg, M. J. Sánchez, R. Weht, C. Acha, F. G. Marlasca, P. Levy, *Phys. Rev. B* **2010**, *81*, 115105.

[26] W. N. Lin, J. F. Ding, S. X. Wu, Y. F. Li, J. Lourembam, S. Shannigrahi, S. J. Wang, T. Wu, *Adv. Mater. Interfaces* **2014**, *1*, 1300001.

[27] D. Yi, J. Liu, S. Okamoto, S. Jagannatha, Y.-C. Chen, P. Yu, Y. H. Chu, E. Arenholz, R. Ramesh, *Phys. Rev. Lett.* **2013**, *111*, 127601.

[28] D. Pesquera, G. Herranz, A. Barla, E. Pellegrin, F. Bondino, E. Magnano, F. Sánchez, J. Fontcuberta, *Nat. Commun.* **2012**, *3*, 1189.

[29] N. B. Aetukuri, A. X. Gray, M. Drouard, M. Cossale, L. Gao, A. H. Reid, H. Alexander, R. Kukreja, H. Ohldag, C. A. Jenkins, E. Arenholz, *Nat. Phys.* **2013**, *9*, 661.

[30] M. Huijben, L. W. Martin, Y. H. Chu, M. B. Holcomb, P. Yu, G. Rijnders, D. H. A. Blank, R. Ramesh, *Phys. Rev. B* **2008**, *78*, 094413.

[31] F. Tsui, M. C. Smoak, T. K. Nath, C. B. Eom, *Appl. Phys. Lett.* **2000**, *76*, 2421.

[32] S. Yoon, K. M. Krishnan, *J. Appl. Phys.* **2011**, *109*, 07B534.

[33] S. R. Bakaul, W. Hu, T. Wu, T. Kimura, *Phys. Rev. B* **2012**, *86*, 184404.

[34] Y. Wu, Y. Suzuki, U. Rüdiger, J. Yu, A. D. Kent, T. K. Nath, C. B. Eom, *Appl. Phys. Lett.* **1999**, *75*, 2295.

[35] S. R. Bakaul, W. Lin, T. Wu, *Appl. Phys. Lett.* **2011**, *99*, 042503.

[36] M. W. Kim, S. J. Moon, J. H. Jung, J. Yu, S. Parashar, P. Murugavel, J. H. Lee, T. W. Noh, *Phys. Rev. Lett.* **2006**, *96*, 247205.

[37] G. A. Gehring, K. A. Gehring, *Rep. Prog. Phys.* **1975**, *38*, 1.

[38] J. Lourembam, J. C. Wu, J. F. Ding, W. N. Lin, T. Wu, *Phys. Rev. B* **2014**, *89*, 014425.